cm CHEMISTRY OF MATERIALS
Communication
Cite This: *Chem. Mater.* 2018, 30, 4503−4507
pubs.acs.org/cm

Structure Determination of a Surface Tetragonal Pt_1Sb_1 Phase on Pt Nanoparticles

Chenliang Ye,[†,‡,∥] Zhenwei Wu,[†,∥] Wei Liu,[§] Yang Ren,[⊥] Guanghui Zhang,[*,†] and Jeffrey T. Miller[*,†]

[†]Davidson School of Chemical Engineering, Purdue University, 480 Stadium Mall Drive, West Lafayette, Indiana 47907, United States
[‡]School of Chemical Engineering and Technology, Tianjin University, Tianjin 300072, China
[§]Dalian Institute of Chemical Physics, Chinese Academy of Sciences, Dalian, Liaoning 116023, China
[⊥]X-ray Science Division, Argonne National Laboratory, 9700 S. Cass Avenue, Lemont, Illinois 60439, United States

Supporting Information

Intermetallic compounds offer the opportunity to obtain new catalysts with enhanced performance in a broad range of reactions compared with their parent monometallic counterparts. The unique properties have inspired increasing investigations into their controlled synthesis, structure−activity relationship, and applications in various areas. Significant advances have been achieved in the past decades, and currently, intermetallic catalysts are widely utilized in many catalytic applications with the Pt−Sn catalyst for naphtha reforming and paraffin dehydrogenation being one successful example.[1−10] Intermetallic nanoparticles usually share the same crystal phases as bulk intermetallic compounds, and phase diagrams can be used to help guide the design and understanding of intermetallic nanocatalysts. However, it has been very challenging to determine the crystal structure of supported intermetallic nanocatalysts due to their small size.[11−18] Recently, with the help of synchrotron X-ray diffraction (XRD), Pt_1Zn_1, Pt_3In and $PtIn_2$ phases have been identified in Pt−Zn and Pt−In dehydrogenation catalysts with ∼2 nm particle size.[11,12] It was proposed that the formation of these intermetallic nanoparticles is kinetically controlled, and it favors the Au_3Cu and AuCu type structures that have relatively high symmetry and require least rearrangement from the parent face-centered cubic (FCC) structure of Pt. For example, Pt−Zn alloys have several possible intermetallic phases, but the Pt_1Zn_1 phase with the AuCu type structure is preferentially formed. Pt−In, Pd−Zn, and Pd−In have also shown similar preferential phase formation in nanoparticles.[19−21] In each of these catalysts, the structure of the nanophase was identical to that of a known bulk alloy.

Although Sb has been extensively used to modify Pt catalysts in methanol/formic acid fuel cells, merely two examples are present in the literature using Pt−Sb bimetallic catalysts in alkane dehydrogenation reaction with controversial conclusions due to the lack of precise understanding of the Pt−Sb alloy phase.[22−26] Interestingly, none of the bulk Pt−Sb intermetallic phases have Au_3Cu or AuCu type structures that are predicted to form according to the hypothesis of kinetically controlled formation of intermetallic nanoparticles. Here we communicate our effort on the synthesis, characterization, and application of a series of Pt−Sb intermetallic nanoparticle catalysts for selective propane dehydrogenation reaction. A AuCu type tetragonal Pt_1Sb_1 phase, which is not known in the bulk materials, was identified using synchrotron *in situ* XRD and X-ray absorption spectroscopy (XAS). Precise determination of the crystal phase led to in-depth understanding toward the structure−function relationship. The high selectivity for propane dehydrogenation of the core−shell nanocatalysts with a Pt core and Pt_1Sb_1 shell ($Pt@Pt_1Sb_1$) can be attributed to the isolation of the active Pt atoms, i.e., a geometric effect that minimizes the hydrogenolysis side reaction. High turnover rates were also observed likely due to the weakened Pt-alkene bonds resulting from the lower energy level of the filled Pt 5d states and higher energy level of the unfilled Pt 5d states compared with monometallic Pt.

A series of Pt−Sb bimetallic nanoparticles were synthesized using sequential impregnation with Sb/Pt molar ratios of 0.5:1, 1:1, 2:1, and 4:1. A monometallic Pt catalyst was synthesized for comparison. The particle sizes are around 2.5 nm with a distribution of ±0.5 nm (Figure S1). Their Pt L3 X-ray absorption near edge structure (XANES) edge energies range from 11564.0 to 11565.5 eV, suggesting that the Pt presents as Pt(0) (Figure 1A). The edge and white line shifted to higher energy with increasing the Sb/Pt ratio indicating the increase of the energy level of the empty Pt 5d states and intermetallic interactions. Three main peaks were observed in the extended X-ray absorption fine structure (EXAFS) spectrum of Pt/SiO_2,

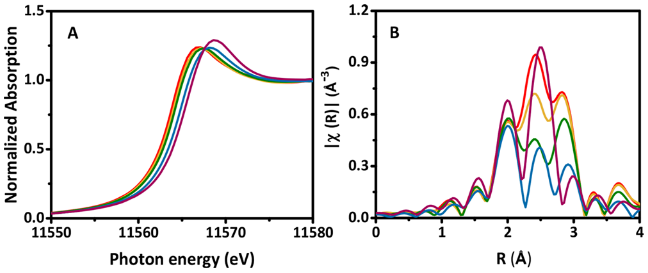

Figure 1. Pt L3 edge XANES (A) and EXAFS (B) spectra. Pt/SiO_2 (red), 0.5Sb−Pt/SiO_2 (yellow) 1Sb−Pt/SiO_2 (olive), 2Sb−Pt/SiO_2 (cyan) and 4Sb−Pt/SiO_2 (wine). FT *k*-range of 3.0−12.0 Å^{-1}, k^2-weighted. All the samples were treated with H_2 at 550 °C.

Received: May 16, 2018
Revised: July 3, 2018
Published: July 9, 2018

ACS Publications

DOI: 10.1021/acs.chemmater.8b02071

typical of metallic Pt–Pt scattering (Figure 1B). As the amount of Sb increases, the peak positions and relative intensities change, consistent with the presence of Sb scatterers within bonding distance. The Pt–Pt coordination number decreased from 8.4 to 5.0, and that of Pt–Sb increased from 0.5 to 3.7 with increasing the Sb:Pt ratio from 0.5:1 to 4:1 (Table 1 and S1). The Pt–Sb distance was ~2.64 Å in all the samples, while the Pt–Pt distance increased from 2.74 Å in 0.5Sb–Pt/SiO_2 to 2.80 Å in 4Sb–Pt/SiO_2. The variation of the Debye–Waller factor of the Pt–Sb path is relatively small (0.003–0.007), whereas that of the Pt–Pt path increased from 0.007 to 0.014, suggesting an increasing disorder of the Pt–Pt path as increasing the Sb:Pt ratio. As shown in Figure S2 and Table S2, the Sb K-edge XANES edge energies and peak intensities of the nanoparticles were very close to those of Sb_2O_3, indicating that most of the Sb in the catalysts remain as Sb(III) after H_2 treatment at 550 °C. In all these samples, there is only a small amount of metallic Sb associated with metallic Pt forming Pt-rich Pt–Sb bimetallic particles, and most of the Sb is present as Sb_2O_3. It is also worth noting that the presence of two isosbestic points at 11567.6 and 111580.0 eV in the XANES spectra (Figure 1A) suggests the formation of a single Pt–Sb phase with varying Sb loadings.

Table 1. Summary of the EXAFS Fitting Results

Sample	Scattering Pairs	C. N.[a]	Distance (Å)	σ^2 (Å^2)
Pt/SiO_2	Pt–Pt	9.7 ± 0.5	2.74 ± 0.01	0.007
0.5Sb–Pt/SiO_2	Pt–Pt	8.4 ± 0.4	2.74 ± 0.01	0.007
	Pt–Sb	0.5 ± 0.2	2.63 ± 0.02	0.003
1Sb–Pt/SiO_2	Pt–Pt	7.6 ± 0.5	2.75 ± 0.01	0.007
	Pt–Sb	1.0 ± 0.3	2.63 ± 0.01	0.004
2Sb–Pt/SiO_2	Pt–Pt	5.2 ± 1.5	2.78 ± 0.01	0.009
	Pt–Sb	2.8 ± 0.5	2.65 ± 0.01	0.007
4Sb–Pt/SiO_2	Pt–Pt	5.0 ± 4.0	2.80 ± 0.02	0.014
	Pt–Sb	3.7 ± 0.7	2.65 ± 0.01	0.005

[a] C. N. = coordination number. Fittings were done using k^2-weighted R-space EXAFS spectra with the k-range of 3.0–12.0 Å^{-1} and the R-range of 1.7–3.2 Å.

Five thermodynamically stable phases of Pt–Sb intermetallic compounds have been reported in the inorganic crystal structure database (ICSD) including Pt_7Sb, Pt_3Sb, Pt_3Sb_2, PtSb, and $PtSb_2$ (Table S3). The Pt–Sb EXAFS distance of ~2.64 Å in the Pt–Sb nanoparticles is not consistent with the formation of Pt_7Sb, Pt_3Sb, or PtSb phase in which the Pt–Sb distances are all longer than 2.75 Å. Formation of Pt_3Sb_2 and/or $PtSb_2$ phases is possible based on the Pt–Sb distances, 2.60–2.68 Å. These phases, however, are not evident from *in situ* synchrotron XRD. As shown in Figure 2A, Pt/SiO_2 showed 4 broad peaks at 2θ of 2.98°, 3.43°, 4.88°, and 5.71° corresponding to the (111), (200), (220), and (311) planes of Pt FCC structure in the 2.5 nm nanoparticle, respectively. With the incorporation of Sb, new overlapping peaks appeared at 2θ of 3.27° and 5.29°, which may be attributed to a Pt–Sb intermetallic or other Sb species. To get narrower and more intense X-ray diffraction peaks for better identification, samples with larger particle sizes (4Sb–Pt/SiO_2-400 and 4Sb–Pt/SiO_2-500, Figure 2B) were synthesized. The XRD patterns do not match any of the known bulk Pt–Sb intermetallic phases, nor metallic Sb (Figure S6 and S7), which suggests the possible formation of a new Pt–Sb phase that has not been reported for bulk materials. The unknown peaks in the XRD patterns of the Pt–Sb catalysts are, therefore, matched by comparing with simulated patterns using the structures with Pt–Sb bond distances from EXAFS fits. The Pt–Sb and Pt–Pt EXAFS distances in 4Sb–Pt/SiO_2 are very similar to those of the Pt–Zn (2.63 Å) and Pt–Pt (2.81 Å) in the tetragonal Pt_1Zn_1 interemtallic phase, which is one of the phases expected to form in such catalysts according to previous studies.[11] The XRD pattern of 4Sb–Pt/SiO_2-500 further suggests possible formation of a tetragonal Pt_1Sb_1 phase (Figure S8).

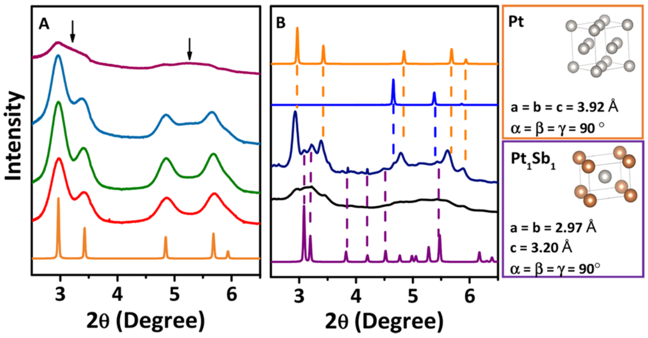

Figure 2. XRD patterns (A) Pt simulation (orange), Pt/SiO_2 (red), 1Sb–Pt/SiO_2 (olive), 2Sb–Pt/SiO_2 (cyan), and 4Sb–Pt/SiO_2 (wine). (B) simulation of the proposed Pt_1Sb_1 alloy (purple), 4Sb–Pt/SiO_2-400 (black), 4Sb–Pt/SiO_2-500 (navy), Sb_2O_3 (blue) and Pt simulation (orange). X-ray energy: 105.715 keV (0.11730 Å).

To assess the possibility of the tetragonal Pt_1Sb_1 phase, the XRD patterns of the tetragonal Pt_1Sb_1 phase were simulated based on the $L1_0$ ordering. A good match was obtained for a bond distance of Pt–Pt at 2.97 Å and Pt–Sb at 2.64 Å in the alloy (Figure 2B). FCC Pt also shows up in the same diffraction pattern, however, its peaks are shifted to a lower angle (~0.02° for the (111) peak), which may result from microstrain due to formation of core–shell structure.[27−30] It should be noted that the relative intensity of the simulated peaks of the proposed Pt_1Sb_1 alloy were different from those of the experimental data. In the simulation, the peak at 3.09° has a higher intensity than that at 3.22°, while in the experimental spectrum, it has a lower intensity possibly due to the presence of a preferred crystallographic orientation in the nanoparticles, likely indicating a two-dimensional surface layer.

To confirm the core–shell structure, high angle annular dark filed (HAADF) image (Figure 3A) was obtained for 2Sb–Pt/

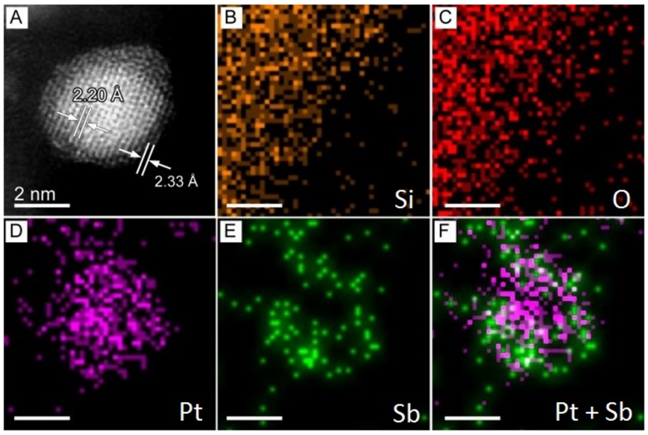

Figure 3. STEM image and EDS analysis of the 2Sb–Pt/SiO_2 catalyst.

SiO_2. The characteristic of atomic number correlated contrast distribution in HAADF offers intuitive demonstration of the delicate core−shell configuration. The brighter core and relatively darker shell correspond to the metallic Pt and tetragonal Pt_1Sb_1 phases, respectively. The spacing in the core is 2.20 Å consistent with the Pt(111) plane, whereas the spacing of outermost two atomic layers of the shell is 2.33 Å, which could be attributed to inevitable surface oxidation during the microcopy study. The high resolution elemental mapping (Figure 3B−F) using energy dispersive X-ray spectroscopy (EDS) analysis provided additional evidence of the composition in this core−shell structure. The Sb atoms are found only in the shell, whereas Pt locates over the entire particle, which reveals the fact of monometallic Pt core as well as the Pt_1Sb_1 alloy shell.

With the Pt_1Sb_1 intermetallic structure identified by *in situ* synchrotron XRD and core−shell geometry revealed by STEM, the EXAFS data of the 2Sb−Pt/SiO_2 and 4Sb−Pt/SiO_2 were refit using a new model including a Pt core and a Pt_1Sb_1 shell in which the Pt−Sb and Pt−Pt distances were fixed as 2.64 and 2.97 Å, respectively. In the new fitting results summarized in Table 2 and S4, the Debye−Waller factors of the surface layer scattering paths including the Pt−Pt at 2.97 Å and Pt−Sb at 2.64 Å are all within the range of 0.004−0.007, which are typical of nanoparticles. The Pt−Pt bond distances in the core increases from 2.74 to2.79 Å, which is consistent with the observed shift to a lower angle of the Pt FCC peaks in the XRD patterns. The Debye−Waller factor of the Pt−Pt path in the core increases from 0.006 to 0.011, consistent with the relatively higher disorder due to the presence of the lattice mismatch between the FCC Pt core and the surface tetragonal Pt_1Sb_1 layer. This also rationalizes the larger Debye−Waller factors (σ^2) and uncertainty of the coordination number in the original EXAFS fitting results which included only one Pt−Pt and one Pt−Sb scattering paths. Fitting the Sb K-edge EXAFS data did not provide useful information on the Sb−Pt bonds due to the presence of large excess of Sb_2O_3.

Table 2. Summary of the EXAFS Fitting Results Using the $Pt@Pt_1Sb_1$ Core−Shell Model[a]

Sample	Scattering pairs	C. N.	Distance (Å)	σ^2 (Å^2)
2Sb−Pt/SiO_2	Pt−Pt	1.1 ± 0.1	2.97 (fixed)	0.006
	Pt−Sb	2.2 ± 0.2	2.64 (fixed)	0.005
	Pt−Pt	6.0 ± 0.6	2.77 ± 0.01	0.008
4Sb−Pt/SiO_2	Pt−Pt	1.6 ± 0.1	2.97 (fixed)	0.007
	Pt−Sb	3.2 ± 0.2	2.64 (fixed)	0.004
	Pt−Pt	4.9 ± 1.2	2.79 ± 0.01	0.011

[a] Fittings were done using k^2-weighted *R*-space spectra with a k-range of 3.0−12.0 Å^{-1} and a *R*-range of 1.7−3.2 Å.

The above results together confirmed the formation of a surface tetragonal Pt_1Sb_1 phase that has not been reported for bulk intermetallic compounds. The fraction of surface Pt in the Pt−Sb bimetallic nanoparticles was determined using CO chemisorption, and the results are summarized in Table 3. The Pt dispersions of Pt/SiO_2, 0.5Sb−Pt/SiO_2, and 1Sb−Pt/SiO_2 are about 30%. Further incorporation of Sb led to a sharp decrease of the Pt dispersion, 11% of 2Sb−Pt/SiO_2 and <0.5% of 4Sb−Pt/SiO_2. Pt dispersions of 2Sb−Pt/SiO_2 and 4Sb−Pt/SiO_2 were lower than the expectation for 2−3 nm particles, suggesting that the surface of the nanoparticles may be covered by excess Sb.

Table 3. Catalytic Dehydrogenation Results[a]

Catalyst	C_3H_6 (%)	CH_4 (%)	C_2H_6 (%)	C_2H_4 (%)	Pt dispersion (%)	TOR (s^{-1})
Pt/SiO_2	24	69	5	2	31	0.4
0.5Sb−Pt/SiO_2	97	2	1	trace	28	0.5
1Sb−Pt/SiO_2	99	trace	trace	trace	28	0.6
2Sb−Pt/SiO_2	99	trace	trace	trace	11	0.6
4Sb−Pt/SiO_2	99	trace	trace	trace	<0.5	–

[a] Reaction conditions: 500 °C, 2% C_3H_8, 3% H_2, and balance N_2. H_2 was cofed to promote the hydrogenolysis side reaction, so that the selectivity can be monitored under severe conditions. The TOR was determined at 10% C_3H_8 conversion based on the first data point at 2 min of time on stream, and the selectivity was determined at 15% C_3H_8 conversion.

These results led to an in-depth understanding of the structure evolution of the $Pt@Pt_1Sb_1$ core−shell nanoparticles. Pt was first reduced to Pt(0), and SbO_x near Pt is reduced at higher temperature. The Sb(0) then diffuses into Pt(0) nanoparticles forming the surface tetragonal Pt_1Sb_1 alloy that requires minimum atomic rearrangement of the Pt FCC structure. The fraction of the Pt_1Sb_1 alloy increases with increasing the Sb loading. This is in contrast to the formation of thermodynamically stable Pt_xSb_y phases which typically requires high temperature where both molten Pt(0) and Sb(0) are slowly cooled. It is worth noting that high Sb loading (Sb/Pt = 4/1) leads to a Sb-covered surface, which is similar to what has been reported for Pd−In alloy nanoparticles where excess In covers the nanoparticle surface.[19]

The surface Pt_1Sb_1 phase efficiently limits hydrogenolysis, which is the side reaction during propane dehydrogenation as summarized in Table 3 and Figure 4. The propylene selectivity of Pt/SiO_2 was 24% at 15% propane conversion. While the propylene selectivity of all the three Pt−Sb catalysts are >97% at 15% propane conversion. The selectivity of 0.5Sb−Pt/SiO_2 maintained ~91%, while catalysts with higher Sb loadings show ~100% selectivity at even higher propane conversion, for example 2Sb−Pt/SiO_2 shows ~100% selectivity even at 36% C_3H_8 conversion (the thermodynamic equilibrium conversion is 46%). The main side reaction, alkane hydrogenolysis, has been suggested to occur on large Pt ensembles. The increased selectivity is consistent with a Pt_1Sb_1 surface alloy, in which each Pt atom is well isolated by surrounding Sb atoms at 2.64

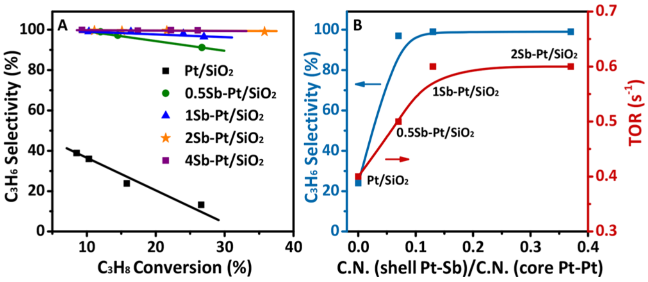

Figure 4. Catalytic performance. (A) C_3H_6 selectivity as a function of C_3H_8 conversion. (B) C_3H_6 selectivity (at 15% C_3H_8 conversion) and dehydrogenation TOR (at 10% C_3H_8 conversion) as a function of shell thickness.

DOI: 10.1021/acs.chemmater.8b02071
Chem. Mater. 2018, 30, 4503−4507

Å, and the shortest Pt−Pt distance is 2.97 Å, which is ∼0.2 Å longer than that in metallic Pt. The hydrogenolysis has been minimized to achieve ∼100% propylene selectivity.

Increasing the Sb/Pt ratio from 0.5:1 to 1:1 further increases the dehydrogenation TOR from 0.5 to 0.6 s^{-1}. Resonant inelastic X-ray scattering (RIXS) and density functional theory (DFT) results suggest higher dehydrogenation TORs can be achieved by weakening the bonds between alkenes and Pt in alloy catalysts with lower energy level of the occupied Pt 5d states and higher energy level of the unoccupied Pt 5d states. In the Pt_1Sb_1 phase, the Pt−Sb distance is 2.64 Å which is much shorter than the sum of the Pt and Sb atomic radius, 2.79 Å, suggesting the presence of strong Pt−Sb bonds. Lower energy level of the filled Pt 5d states and higher energy level of the unfilled 5d states would be expected, latter of which is consistent with the XANES shift to higher energy. The change of the energy levels in the Pt_1Sb_1 surface alloy is believed to be responsible for the higher TORs in propane dehydrogenation. Such understanding of the structure-selectivity relation could not be obtained without the detailed picture of the surface structure of the Pt−Sb nanoparticles.

In summary, a new tetragonal Pt_1Sb_1 phase not known in phase diagram was evidenced in 2−3 nm core−shell nanoparticle catalysts by *in situ* synchrotron XAS, XRD, HAADF imaging, and EDS analysis. A kinetically controlled diffusion of Sb(0) into Pt(0) nanoparticles with minimum atomic rearrangement of the FCC Pt structure was proposed to explain the formation of this unique phase on top of a Pt core at the nanoscale. In the Pt_1Sb_1 surface alloy, strong Pt−Sb bonds are formed with a bond distance of 2.64 Å. Each Pt atom is isolated by Sb atoms, and thus the Pt_1Sb_1 alloy exhibits high selectivity in propane dehydrogenation reaction resulting from the geometric effect that minimizes the hydrogenolysis side reaction. This work highlights the importance of fundamental understanding of the precise structure of the surface layer in supported small nanoparticle catalysts (<3 nm in size) toward rational design of new core−shell nanoparticle catalysts.

■ ASSOCIATED CONTENT

Ⓢ Supporting Information

The Supporting Information is available free of charge on the ACS Publications website at DOI: 10.1021/acs.chemmater.8b02071.

Experimental details, STEM images, and detailed EXAFS fitting results and XRD simulations (PDF)

■ AUTHOR INFORMATION

Corresponding Authors

*G. Zhang. E-mail: zhan2739@purdue.edu.
*J. T. Miller. E-mail: mill1194@purdue.edu.

ORCID

Guanghui Zhang: 0000-0002-5854-6909
Jeffrey T. Miller: 0000-0002-6269-0620

Author Contributions

[‖]These authors contributed equally.

Notes

The authors declare no competing financial interest.

■ ACKNOWLEDGMENTS

Z.W., G.Z., and J.T.M. were supported in part by the National Science Foundation under Cooperative Agreement No. EEC-1647722. Any opinions, findings, and conclusions or recommendations expressed in this material are those of the author(s) and do not necessarily reflect the views of the National Science Foundation. C.Y. thanks the financial support from the Chinese Scholarship Council (CSC). Use of the Advanced Photon Source was supported by the U.S. Department of Energy, Office of Basic Energy Sciences [grant number DE-AC02-06CH11357]. MRCAT operations, beamline 10-BM, are supported by the Department of Energy and the MRCAT member institutions. The authors also acknowledge the use of beamline 11-ID-C.

■ REFERENCES

(1) Yu, W.; Porosoff, M. D.; Chen, J. G. Review of Pt-Based Bimetallic Catalysis: From Model Surfaces to Supported Catalysts. *Chem. Rev.* **2012**, *112*, 5780−5817.

(2) De, S.; Zhang, J.; Luque, R.; Yan, N. Ni-based Bimetallic Heterogeneous Catalysts for Energy and Environmental Applications. *Energy Environ. Sci.* **2016**, *9*, 3314−3347.

(3) Sankar, M.; Dimitratos, N.; Miedziak, P. J.; Wells, P. P.; Kiely, C. J.; Hutchings, G. J. Designing Bimetallic Catalysts for A Green and Sustainable Future. *Chem. Soc. Rev.* **2012**, *41*, 8099−8139.

(4) Vora, B. V. Development of Dehydrogenation Catalysts and Processes. *Top. Catal.* **2012**, *55*, 1297−1308.

(5) Xiong, H.; Lin, S.; Goetze, J.; Pletcher, P.; Guo, H.; Kovarik, L.; Artyushkova, K.; Weckhuysen, B. M.; Datye, A. K. Thermally Stable and Regenerable Platinum−Tin Clusters for Propane Dehydrogenation Prepared by Atom Trapping on Ceria. *Angew. Chem., Int. Ed.* **2017**, *56*, 8986−8991.

(6) Furukawa, S.; Komatsu, T. Intermetallic Compounds: Promising Inorganic Materials for Well-Structured and Electronically Modified Reaction Environments for Efficient Catalysis. *ACS Catal.* **2017**, *7*, 735−765.

(7) Gao, F.; Goodman, D. W. Pd-Au Bimetallic Catalysts: Understanding Alloy Effects from Planar Models and (supported) Nanoparticles. *Chem. Soc. Rev.* **2012**, *41*, 8009−8020.

(8) Wang, X.; Altmann, L.; Stöver, J.; Zielasek, V.; Bäumer, M.; Al-Shamery, K.; Borchert, H.; Parisi, J.; Kolny-Olesiak, J. Pt/Sn Intermetallic, Core/Shell and Alloy Nanoparticles: Colloidal Synthesis and Structural Control. *Chem. Mater.* **2013**, *25*, 1400−1407.

(9) Lei, Y.; Liu, B.; Lu, J.; Lobo-Lapidus, R. J.; Wu, T.; Feng, H.; Xia, X.; Mane, A. U.; Libera, J. A.; Greeley, J. P.; Miller, J. T.; Elam, J. W. Synthesis of Pt−Pd Core−Shell Nanostructures by Atomic Layer Deposition: Application in Propane Oxidative Dehydrogenation to Propylene. *Chem. Mater.* **2012**, *24*, 3525−3533.

(10) Srinivasan, R.; Sharma, R.; Su, S.; Davis, B. H. Crystalline Phases in Pt-Sn Bimetallic Catalysts: a High Resolution Electron Microscopy Study. *Catal. Today* **1994**, *21*, 83−99.

(11) Cybulskis, V. J.; Bukowski, B. C.; Tseng, H.-T.; Gallagher, J. R.; Wu, Z.; Wegener, E.; Kropf, A. J.; Ravel, B.; Ribeiro, F. H.; Greeley, J.; Miller, J. T. Zinc Promotion of Platinum for Catalytic Light Alkane Dehydrogenation: Insights into Geometric and Electronic Effects. *ACS Catal.* **2017**, *7*, 4173−4181.

(12) Wegener, E. C.; Wu, Z.; Tseng, H.-T.; Gallagher, J. R.; Ren, Y.; Diaz, R. E.; Ribeiro, F. H.; Miller, J. T. Structure and Reactivity of Pt−In Intermetallic Alloy Nanoparticles: Highly Selective Catalysts for Ethane Dehydrogenation. *Catal. Today* **2018**, *299*, 146−153.

(13) Redekop, E. A.; Galvita, V. V.; Poelman, H.; Bliznuk, V.; Detavernier, C.; Marin, G. B. Delivering a Modifying Element to Metal Nanoparticles via Support: Pt−Ga Alloying during the Reduction of $Pt/Mg(Al,Ga)O_x$ Catalysts and Its Effects on Propane Dehydrogenation. *ACS Catal.* **2014**, *4*, 1812−1824.

(14) Ballarini, A. D.; de Miguel, S. R.; Castro, A. A.; Scelza, O. A. n-Decane Dehydrogenation on Pt, PtSn and PtGe Supported on Spinels

Prepared by Different Methods of Synthesis. *Appl. Catal., A* **2013**, *467*, 235−245.

(15) Sattler, J. J. H. B.; Gonzalez-Jimenez, I. D.; Luo, L.; Stears, B. A.; Malek, A.; Barton, D. G.; Kilos, B. A.; Kaminsky, M. P.; Verhoeven, T. W. G. M.; Koers, E. J.; Baldus, M.; Weckhuysen, B. M. Platinum-Promoted Ga/Al_2O_3 as Highly Active, Selective, and Stable Catalyst for the Dehydrogenation of Propane. *Angew. Chem., Int. Ed.* **2014**, *53*, 9251−9256.

(16) Wang, T.; Jiang, F.; Liu, G.; Zeng, L.; Zhao, Z. j.; Gong, J. Effects of Ga Doping on Pt/CeO_2-Al_2O_3 Catalysts for Propane Dehydrogenation. *AIChE J.* **2016**, *62*, 4365−4376.

(17) Liu, G.; Zeng, L.; Zhao, Z.-J.; Tian, H.; Wu, T.; Gong, J. Platinum-Modified ZnO/Al_2O_3 for Propane Dehydrogenation: Minimized Platinum Usage and Improved Catalytic Stability. *ACS Catal.* **2016**, *6*, 2158−2162.

(18) Galvita, V.; Siddiqi, G.; Sun, P.; Bell, A. T. Ethane Dehydrogenation on Pt/Mg (Al) O and PtSn/Mg (Al) O Catalysts. *J. Catal.* **2010**, *271*, 209−219.

(19) Wu, Z.; Wegener, E. C.; Tseng, H.-T.; Gallagher, J. R.; Harris, J. W.; Diaz, R. E.; Ren, Y.; Ribeiro, F. H.; Miller, J. T. Pd−In Intermetallic Alloy Nanoparticles: Highly Selective Ethane Dehydrogenation Catalysts. *Catal. Sci. Technol.* **2016**, *6*, 6965−6976.

(20) Childers, D. J.; Schweitzer, N. M.; Shahari, S. M. K.; Rioux, R. M.; Miller, J. T.; Meyer, R. J. Modifying Structure-Sensitive Reactions by Addition of Zn to Pd. *J. Catal.* **2014**, *318*, 75−84.

(21) Gallagher, J. R.; Childers, D. J.; Zhao, H.; Winans, R. E.; Meyer, R. J.; Miller, J. T. Structural Evolution of an Intermetallic Pd−Zn Catalyst Selective for Propane Dehydrogenation. *Phys. Chem. Chem. Phys.* **2015**, *17*, 28144−28153.

(22) Yu, X.; Pickup, P. G. Pb and Sb Modified Pt/C Catalysts for Direct Formic Acid Fuel Cells. *Electrochim. Acta* **2010**, *55*, 7354−7361.

(23) Yu, X.; Pickup, P. G. Codeposited PtSb/C Catalysts for Direct Formic Acid Fuel Cells. *J. Power Sources* **2011**, *196*, 7951−7956.

(24) Pan, C.; Li, Y.; Ma, Y.; Zhao, X.; Zhang, Q. Platinum−Antimony Doped Tin Oxide Nanoparticles Supported on Carbon Black as Anode Catalysts for Direct Methanol Fuel Cells. *J. Power Sources* **2011**, *196*, 6228−6231.

(25) Asakura, K.; Okumura, K.; Inoue, T.; Kubota, T.; Chun, W. J.; Iwasawa, Y. Chemical Control of Noble Metal Catalysis by Main Group Elements. *MRS Online Proc. Libr.* **1997**, *497*, 99−108.

(26) Cheng, C. H.; Dooley, K. M.; Price, G. L. The Role of Tellurium and Antimony in $PtTeAl_2O_3$ and $PtSbAl_2O_3$ Reforming Catalysts. *J. Catal.* **1989**, *116*, 325−337.

(27) Strasser, P.; Koh, S.; Anniyev, T.; Greeley, J.; More, K.; Yu, C.; Liu, Z.; Kaya, S.; Nordlund, D.; Ogasawara, H.; et al. Lattice-strain Control of the Activity in Dealloyed Core−shell Fuel Cell Catalysts. *Nat. Chem.* **2010**, *2*, 454−460.

(28) Chen, X.; Lou, Y.; Samia, A. C.; Burda, C. Coherency Strain Effects on The Optical Response of Core/shell Heteronanostructures. *Nano Lett.* **2003**, *3*, 799−803.

(29) Montazeri, M.; Fickenscher, M.; Smith, L. M.; Jackson, H. E.; Yarrison-Rice, J.; Kang, J. H.; Gao, Q.; Tan, H. H.; Jagadish, C.; Guo, Y.; et al. Direct Measure of Strain and Electronic Structure in GaAs/GaP Core− Shell Nanowires. *Nano Lett.* **2010**, *10*, 880−886.

(30) Kar, A.; Patra, A. Impacts of Core−shell Structures on Properties of Lanthanide-based Nanocrystals: Crystal Phase, Lattice Strain, Downconversion, Upconversion and Energy Transfer. *Nanoscale* **2012**, *4*, 3608−3619.